Materials Characterization 197 (2023) 112676

Contents lists available at ScienceDirect

Materials Characterization

journal homepage: www.elsevier.com/locate/matchar

Analysis of (Al,Cr,Nb,Ta,Ti)-nitride and -oxynitride diffusion barriers in Cu-Si interconnects by 3D-Secondary Ion Mass Spectrometry

Andreas Kretschmer [a,*], Fabian Bohrn [a,b], Herbert Hutter [b], Eduardo Pitthan [c], Tuan Thien Tran [c], Daniel Primetzhofer [c], Paul Heinz Mayrhofer [a]

[a] Institute of Materials Science and Technology, TU Wien, Gumpendorferstraße 7, 1060 Vienna, Austria
[b] Institute of Chemical Technologies and Analytics, TU Wien, Getreidemarkt 9, 1060 Vienna, Austria
[c] Department of Physics and Astronomy, Uppsala University, SE-75120 Uppsala, Sweden

ARTICLE INFO

Keywords:
Vapor deposition
Diffusion
Ceramics
Entropy

ABSTRACT

We report on the barrier performance of a nitride, and three oxynitrides of the system Al-Cr-Nb-Ta-Ti between Cu and Si. Different high-entropy sublattice nitrides have been tested before as diffusion barriers in this system, by depositing thin barriers on single crystalline Si substrates, followed by a thick Cu layer on top, and subsequent vacuum annealing. We investigated a reversed stacking sequence, by sputtering 15–30 nm of (Al,Cr,Nb,Ta,Ti)-O-N (between 0.5 and 63.7 at.% O) on polished polycrystalline Cu substrates, followed by 200 nm of Si. The samples were then vacuum annealed at 600, 700, 800 and 900 °C for 30 min. All four investigated coatings perform similar. Secondary Ion Mass Spectrometry depth profiling in high-current-bunched mode (lateral resolution ± 1 μm) shows breakthrough of Si even at 600 °C. But 3D constructed images with Burst Alignment mode (lateral resolution of ±2 *nm*) reveal that this failure is a highly localized phenomenon, likely related to coarsening effects at the Cu grain boundaries, leading to punctuation of the diffusion barrier. Aside from this penetration, the majority of the area of each barrier coating retains its function. This in-depth analysis shows that the barrier function of the nitride and oxynitride coatings mostly stays intact up to 800 °C and fails completely at 900 °C.

1. Introduction

Modern interconnects in semiconductor devices bring the two elements Cu and Si into close contact. The diffusion of these elements and the following formation of intermetallic phases like Cu_3Si with high specific resistance leads to degradation of the semiconductor device with time. Therefore, diffusion barriers are applied to separate the elements. To satisfy the demand of increasing computational power, the structures in semiconductor devices become ever smaller, driving the development of improved diffusion barriers [1]. Many different materials have been investigated as diffusion barriers, among these metals like Ta [2,3], or ceramics such as nitrides [4–6] or oxides [7]. Ru was successfully added to some barriers, improving the breakthrough resistance [8,9]. Since diffusion is greatly accelerated at grain boundaries, and the aforementioned materials have a tendency to crystallize in columnar structures either during the PVD process or at a later stage, fast-track diffusion soon defeats the purpose of the barrier. Amorphous materials do not offer such a diffusion pathway and thus show better retention performance. High-entropy alloys (HEA) [10,11], consisting of five or more atoms in equiatomic or near-equiatomic composition, placed randomly on a crystalline lattice, were quickly recognized as prime candidates for diffusion barriers due to their strong lattice distortion. It was also proposed that high-entropy materials are stabilized by their configurational entropy and that diffusion in them is sluggish [12], but the generality of these statements has been disputed [13–17]. Nevertheless, the atomic size mismatch retards the recrystallization in HEA (through the known solution drag [18]), so that they have been applied successfully as diffusion barriers [19–22]. The great performance of the respective nitrides of such HEA – labeled high-entropy sublattice nitrides (HESN) to reflect the entropic contributions correctly [23,24] – have also been demonstrated numerous times [25–31], owing to their great thermal stability. Another successful

* Corresponding author at: TU Wien, Institute of Materials Science and Technology E308, Gumpendorferstrasse 7, 1060 Vienna, Austria.
E-mail addresses: andreas.kretschmer@tuwien.ac.at (A. Kretschmer), fabian.bohrn@tuwien.ac.at (F. Bohrn), herbert.hutter@tuwien.ac.at (H. Hutter), eduardo.pitthan@physics.uu.se (E. Pitthan), tuan.tran@physics.uu.se (T.T. Tran), daniel.primetzhofer@physics.uu.se (D. Primetzhofer), paul.mayrhofer@tuwien.ac.at (P.H. Mayrhofer).

https://doi.org/10.1016/j.matchar.2023.112676
Received 3 November 2022; Accepted 11 January 2023
Available online 18 January 2023
1044-5803/© 2023 The Authors. Published by Elsevier Inc. This is an open access article under the CC BY license (http://creativecommons.org/licenses/by/4.0/).

strategy is the deposition of multilayer barrier structures [32–35].

These previous works focused almost exclusively on different metal compositions, while the non-metal sublattice in ceramics has received only little attention in the form of N vacancies. It has been shown in Al-Ti-N that O incorporation improves the thermal stability and reduces the self-diffusion [36], thus alloying of the non-metal sublattice is promising for diffusion applications. Here, we compare the performance of diffusion barriers with identical metal-sublattice occupations, but varying non-metal lattices in the system (Al,Cr,Nb,Ta,Ti)-O-N. This material has been shown to form a stable single-phase face-centered-cubic solid solution as nitride [37], and also a single-phase solid solution in rutile-structure as oxide [38]. This system is therefore a promising candidate for mixed non-metal sublattices.

The previous studies on diffusion barriers in Cu-Si interconnects have all been conducted on single-crystalline Si substrates, by depositing the thin diffusion barrier on top, followed by a several hundred nanometer thick Cu layer. Sputtering Cu is problematic, because the Cu vapors contaminate the vacuum pumps, and pose a health risk, leading to exceedingly expensive maintenance procedures. Additionally, growing amorphous films on Si (with the native oxide at the surface) – especially at low temperatures and only few nm thick – is straight forward. This is even valid for materials that easily crystallize such as TiN [27]. However, growing the same films on metallic substrates such as Cu easily causes their crystallization. Thus, if the films are amorphous when grown on Cu, this proves their ability for amorphization. We therefore explored the feasibility of a reverse stacking sequence to study diffusion phenomena in this model system, using Cu as substrate, and depositing Si on top of the barrier. While this method does not reflect the common procedures in semiconductor production, it is suitable to study the underlying diffusion phenomena. We thus avoid the problem of sputtering Cu and simultaneously assess the capability of amorphous growth of the barriers on a metallic substrate. We then monitored the diffusion of Si in the Cu with Secondary Ion Mass Spectrometry (SIMS).

2. Methods

2.1. Deposition

Depositions were performed in an AJA International Orion 5 magnetron sputtering system using a powdermetallurgically prepared equimolar 3″ AlCrNbTaTi and a 2″ Si target (both from Plansee Composite Materials GmbH) in a con-focal arrangement. The substrates, (100) oriented Si single crystals, polycrystalline austenitic steel, and polycrystalline Cu, cut and polished from used vacuum sealing rings, were ultrasonically cleaned in acetone and ethanol for 5 min each, and placed in the deposition chamber via a load-lock.

After waiting for a base pressure of $< 3 \times 10^{-4}$ Pa, the substrates were cleaned by Ar plasma etching for 60 min by applying a negative bias potential of -900 V to the substrates at an Ar pressure of 6 Pa. During the last 5 min of the plasma etching, the targets were cleaned by sputtering behind the closed shutter. In the last minute before opening the shutter, the gas composition was adjusted to the respective $Ar/N_2/O_2$ mixtures at a total pressure of 0.4 Pa. The substrates were mounted 110 mm above the targets. The (Al,Cr,Nb,Ta,Ti) N/ON layer was deposited by supplying 150 W to the cathode in DC mode, a substrate bias of -100 V ensured a compact layer. The four different barriers were realized by sputtering in gas ratios of N_2/synthetic air/Ar of 4.5/0/5.5, 4.0/0.5/5.5, 3.5/1.0/5.5, and 0/4.5/5.5, respectively, for 42.5, 36, 44.5, and 97.8 s, respectively, to deposit roughly 10 nm thin layers. The nitride and oxynitride layers were then covered by 200 nm Si by supplying 100 W to the Si cathode in 10 sccm Ar flow at the same pressure for 45 min without bias. This ensured a stacking sequence of Cu/HESN/Si without contamination at the interface. The required deposition times were determined by preliminary testing of the parameters. Synthetic air was used instead of O_2 to reach lower flow rate ratios $f = f_{O_2}/(f_{O_2} + f_{N_2})$. The samples were not heated during deposition.

2.2. Analysis

Depth profiles of the chemical composition were determined on the ≈1 μm thick reference coatings on Si by time-of-flight elastic recoil detection analysis (ToF-ERDA) with a recoil detection angle of 45° using a beam of 36 MeV I^{8+} ions. For the experimental details, data analysis, and potential systematic uncertainties see [39–42]. Deposited Cu/HESN/Si stacks were vacuum annealed in a vacuum below $3{\cdot}10^{-6}$ mbar for 30 min in a Centorr LF22-2000 vacuum furnace at $T_a = 600, 700, 800,$ and 900 °C. The heating rate was 20 K/min, passive cooling (at least 50 K/min down to 200 °C) was used to cool down. Structure investigations were performed with X-ray-diffraction (XRD) using a PANanlytical XPert Pro MPD ($\theta - \theta$ diffractometer) in Bragg–Brentano geometry equipped with a Cu-Kα source ($\lambda = 0.15408$ nm, 45 kV and 40 mA). Transmission electron microscopy (TEM) was performed with a FEI TECNAI F20, equipped with a FEG, operated at 200 kV, on as-deposited and annealed samples. The sheet resistance of the ≈1 μm thick coatings on Si was measured with the four-point probe method, in which a constant current is injected through the two outer probes and the potential is measured between the two inner probes. Depending on the resistivity of the material, the injected current is chosen automatically from 10 mA to 10 nA by the system to obtain an optimal measurement. The acceptance threshold between forward and backward measurement was 5%.

The spatial distribution of Si before and after annealing was analyzed by Time-of-Flight Secondary Ion Mass Spectrometry (SIMS), using a TOF-SIMS 5 instrument (IONTOF GmbH, Münster, Germany). Depth profiles were acquired in high vacuum ($\sim 4 \times 10^{-9}$mbar) using a pulsed 25 keV Bi^+ primary ion beam for analysis, and a 2 keV Cs source as sputter gun. The measurements were performed in interlaced mode, generating spectra with the Bi gun in 0.7 ns long time windows, followed by 100 μs spectrum acquisition time, during which the sputter gun removed roughly one monolayer of material. Two different measurement modes were used. High current bunched mode (HCBU) was used for measurements which require a high mass resolution or low limit of detection. For imaging and 3D modeling, the burst alignment (BA) mode was used [43–46]. In HCBU mode, the analysis area was set to 100×100 μm^2 with a resolution of 128×128 px^2 with 1 shot/pixel. The measurement was stopped after 1800 s. For imaging in BA mode, the interlaced mode was used as well (the signal intensity is ≈ 6 times smaller than in spectrometry), with an analysis area of 100×100 μm^2 at a resolution of 256×256 px. The sputter crater (using Cs ions) was always 300×300 μm^2. Low energy electron flooding of 21 V was used to reduce surface charging.

To acquire the actual sputter depth, a stylus profilometer Dektak XT (Bruker Corporation, Billerica, MA, USA) was used. Several line scans were performed through the center of the crater and the average depth in the middle of the crater was calculated. This information was then used with the SurfaceLab 7 software (IONTOF GmbH, Münster, Germany) to calibrate the z-axis of the measurement. Furthermore, in SurfaceLab 7 the three dimensional elemental distribution cubes were calculated and exported to Origin9 software.

3. Results and discussion

3.1. Barrier chemistry and morphology

The chemical composition was evaluated on separately deposited ≈1 μm thick samples by ToF-ERDA, the respective depth profiles of the four compositions are shown in Fig. 1a), the changes in composition with different flow rate ratios f is shown in Fig. 1e) and and listed in Table 1. The compositions were obtained from the average compositions in the regions of quantification, shown in Fig. 1. These regions were chosen to exclude influence from the surface due to air exposition, and multiple scattering at greater depths that affect the analysis (see [42] for more details). These measured bulk-like compositions may deviate from

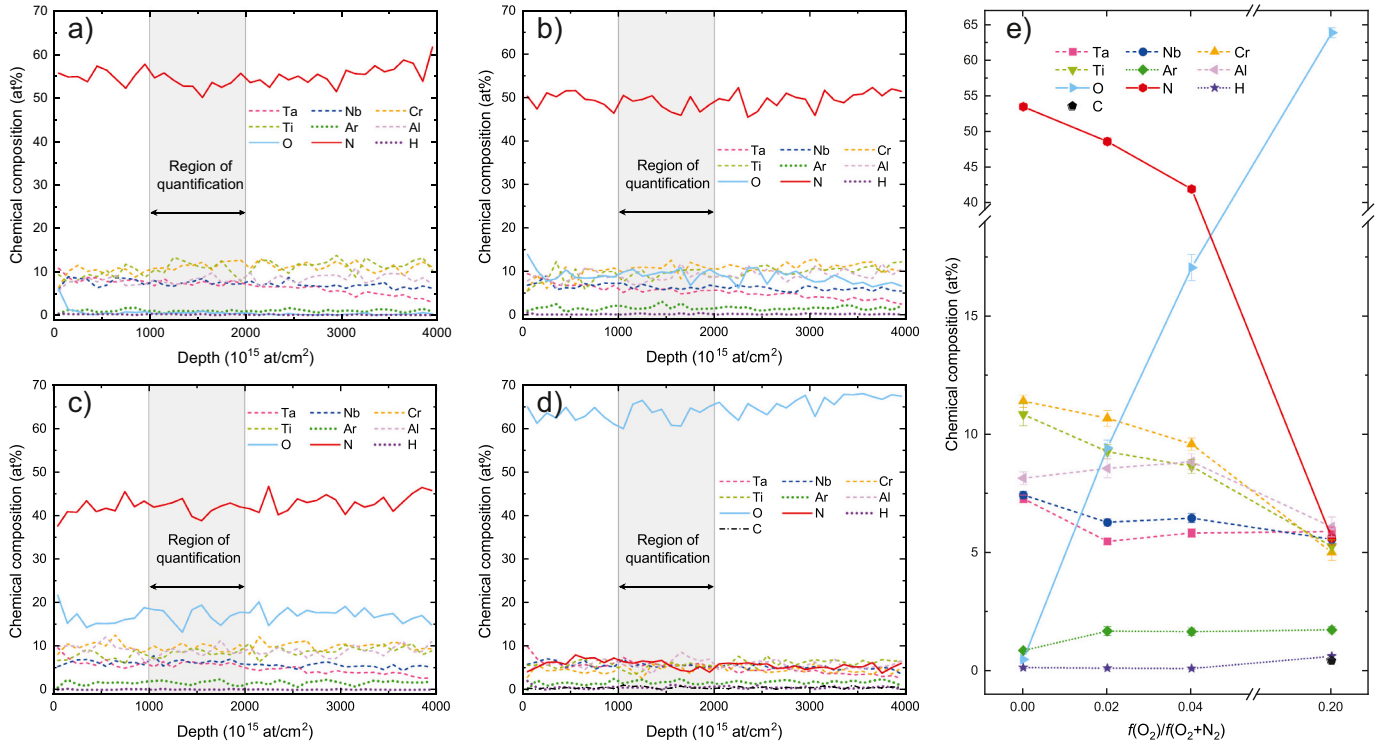

Fig. 1. ERDA depth profiles of the nitride and oxynitrides, deposited with flow rate ratios $f_{O_2}/(f_{O_2}+f_{N_2}) = 0.000$ a), 0.022 b), 0.044 c), and 0.200 d), measured on ≈1 μm thick coatings, deposited separately on Si. The depth from 1000 to 2000 × 10^{15} at/cm^2, highlighted in gray, was used for quantification. The dependence of composition on the the gas flow rates is depicted in e) with statistical uncertainties shown as error bars.

Table 1
Chemical Analysis in at.% by ToF-ERDA. Samples are identified by the flow rate ratio $f = f_{O_2}/(f_{O_2}+f_{N_2})$ Statistical uncertainties are given as standard errors. Configurational entropies are calculated with the sublattice model [13] and given for the metal sublattice, M, non-metal sublattice (counting O and N), NM, and their combination Σ.

	Chemical composition in at.%										S_{conf}/R		
f	Al	Cr	Nb	Ta	Ti	N	O	Ar	H	C	M	NM	Σ
0.000	8.1 ± 0.3	11.4 ± 0.3	7.4 ± 0.2	7.3 ± 0.2	10.8 ± 0.5	53.4 ± 0.5	0.5 ± 0.1	0.9 ± 0.1	0.1 ± 0.0		1.59	0.05	0.75
0.022	8.6 ± 0.4	10.7 ± 0.3	6.3 ± 0.2	5.5 ± 0.1	9.3 ± 0.3	48.5 ± 0.5	9.4 ± 0.3	1.7 ± 0.2	0.1 ± 0.0		1.58	0.44	0.91
0.044	8.8 ± 0.3	9.6 ± 0.3	6.5 ± 0.2	5.8 ± 0.2	8.6 ± 0.3	41.8 ± 0.4	17.0 ± 0.6	1.7 ± 0.2	0.1 ± 0.0		1.59	0.60	1.00
0.200	6.1 ± 0.4	5.0 ± 0.3	5.6 ± 0.2	5.9 ± 0.2	5.3 ± 0.3	5.6 ± 0.3	63.8 ± 0.7	1.7 ± 0.1	0.6 ± 0.1	0.4 ± 0.1	1.61	0.28	0.66

the compositions at the interface, but the analysis of thicker coatings was motivated by the long transport from the sputtering chamber to the particle accelerator. In the nitride, the Cr and Ti contents are around 11 at.%, while the Nb and Ta contents are lower around 7.4 at.% and the Al content is 8.1 ± 0.3 at.%. The N content is slightly overstoichiometric with 53.4 ± 0.5 at.%, in addition, O, Ar, and H impurities below 1 at.% each were found. These values are consistent with the investigations in [37] and the concentrations add up to a HESN with roughly 1:1 stoichiometry as one would expect of a typical transition metal nitride. With the addition of O_2 to the sputter gas, the relative abundance of the metals changes, the share of Cr and Ti on the metal sublattice decreases from 25 and 24%, in the nitride, to 18 and 19%, respectively, at the highest O-content. The shares of Al, Nb, and Ta increase from 18, 17, and 16% to 22, 20, and 21%, respectively, with rising O-content. The oxidic coating was also the only one with a detectable amount of C. Since only the sputter gas was changed between the depositions, whereas the target was powdermetallurgically prepared, the relative changes in chemistry stem from different poisoning behavior of the individual target subgrains in the Ar/N_2 atmosphere, or the $Ar/N_2/O_2$ atmosphere. Oxides have a higher binding energy, resulting in stronger poisoning effects and reduced sputter rates. Thus, Cr and Ti could either show stronger poisoning by oxygen, or less poisoning by the N-atmosphere compared to the other metals (both AlN and Al_2O_3 are insulating, while the transition metal nitrides generally possess metallic character).

With addition of O, the stoichiometry of the coating changes gradually. The nitride at 53.9 at.% (N + O) content resembles a nitride with slightly overstoichiometric 1:1 metal:non-metal ratio. With increasing O content, the amount of nonmetal content rises up to 69.4 at.%. Since at a high O content, the sample contains only 5.6 at.% N, the coating resembles a slightly overstoichiometric MO_2 compound, which agrees with sputtered coatings of this system in oxygen atmosphere [38]. The four different compositions will be differentiated throughout this article as $(Al,Cr,Nb,Ta,Ti)_{0.45}N_{0.55}$, $(Al,Cr,Nb,Ta,Ti)_{0.40}N_{0.49}O_{0.10}$, $(Al,Cr,Nb,Ta,Ti)_{0.39}N_{0.42}O_{0.17}$, and $(Al,Cr,Nb,Ta,Ti)_{0.28}N_{0.06}O_{0.64}$. The configurational entropy of the metal sublattice – ignoring the minuscule amounts of Ar, H, and C – is between 1.58 and 1.61·R in all coatings, therefore fulfilling the definition of a high-entropy sublattice ceramic. The overall configurational entropy, across both sublattices, can be calculated according to the sublattice model [13]

$$\Delta S_{conf} = -R\left(\sum_{j=1}^{J} a^j \sum_{i=1}^{n} x_i^j \ln x_i^j\right) \Big/ \sum_{j=1}^{J} a^j, \quad (1)$$

where x_i^j is the concentration of the ith element on the jth sublattice, a^j is

the number of sites on the *j*th sublattice (e.g. for TiO_2 $a^{Ti}=1$ and $a^{O}=2$), and *n* is the number of element species *i* at the sublattice. Based on this approximation, the overall configurational entropy increases in the fcc structured oxynitrides (see the XRD analysis below) from 0.75 to 1.00·*R*, in the coating with the highest oxygen content it decreases to 0.66·*R* (see Table 1). The sheet resistance of the coatings could only be evaluated qualitatively, because the Si substrate conducts a significant fraction of the current. Despite this, a clear trend is evident with sheet resistances increasing from 5 to 62, and 201 Ω/sq with increasing O content, while the sample with the highest O-content was out of the measurement range of the instrument. Therefore, even small amounts of O in the barrier are detrimental for the electrical conductivity in interconnects.

The stacking sequence on Cu is clearly visible in TEM, see Fig. 2 a)-b) and c)-d) for bright-field and high-resolution micrographs of as deposited $(Al,Cr,Nb,Ta,Ti)_{0.45}N_{0.55}$ and $(Al,Cr,Nb,Ta,Ti)_{0.28}N_{0.06}O_{0.64}$, respectively. For both coatings, we see a high surface quality of the polished Cu substrate, followed by the barrier layer, which is 15 nm thick in the case of the nitride, and 30 nm thick for the oxidic coating, while the Si is ≈200 nm thick. Based on the sputter parameters we can expect similar thicknesses around 15 nm for the other two coatings. This is slightly more than our aim of 10 nm, but still within a reasonable range for diffusion studies. The deposition rates were calibrated by measuring the thicknesses of coatings deposited for 30 min. The discrepancy between actual and calibrated film thickness, excluding Si, hints at a stabilization to a steady-state during the first minute of deposition, resulting in deviating deposition rates. The high-resolution images in Fig. 2 b) and d) show the clear transition between the layers without significant contamination at the interfaces, also confirmed by EDS-linescans. Fast Fourier transformations (FFT) of regions inside the Cu, the barriers, and the Si, shown in the insets of Fig. 2 b) and d), reveal crystalline features inside the Cu substrate, seen by the distinct spots, while the diffusion barriers and the Si are amorphous, as seen by the diffuse rings in their FFT. This setup promises good resistance against diffusion, since grain boundaries in the barrier would lead to much faster grain-boundary diffusion.

In Fig. 3 a) XRD scans of the ≈1 μm thick coatings on austenitic steel substrates are shown with increasing O content from bottom to top. The coatings with up to 17.0 at.% O show crystalline fcc peaks with a lattice parameter similar to TiN. Since austenitic steel and Cu have the same crystal structure and very similar lattice parameters of 3.5922 Å (PDF number 00–047-1405) and 6.6022 Å (PDF number 04–009-2090), respectively, we can expect them to behave very similar as substrates. Thus, the coatings on the steel substrate have crystallized due to the higher coating thickness, while the few nanometer thin films on the structurally similar Cu substrate remain amorphous. The coating with the highest O content is XRD amorphous, signified by the broad feature around 27°, showing that the crystallization of the predominantly oxidic coating requires higher deposition temperatures compared to the nitride (no heating was used). Contrary to the thicker coatings, the N-rich coatings are amorphous when prepared as thin barriers, as confirmed by TEM. Since TEM has shown that the barrier layers are amorphous both at the highest and lowest oxygen concentration, we can expect the other two barrier compositions to also form amorphous structures in the thin layer, as confirmed by XRD.

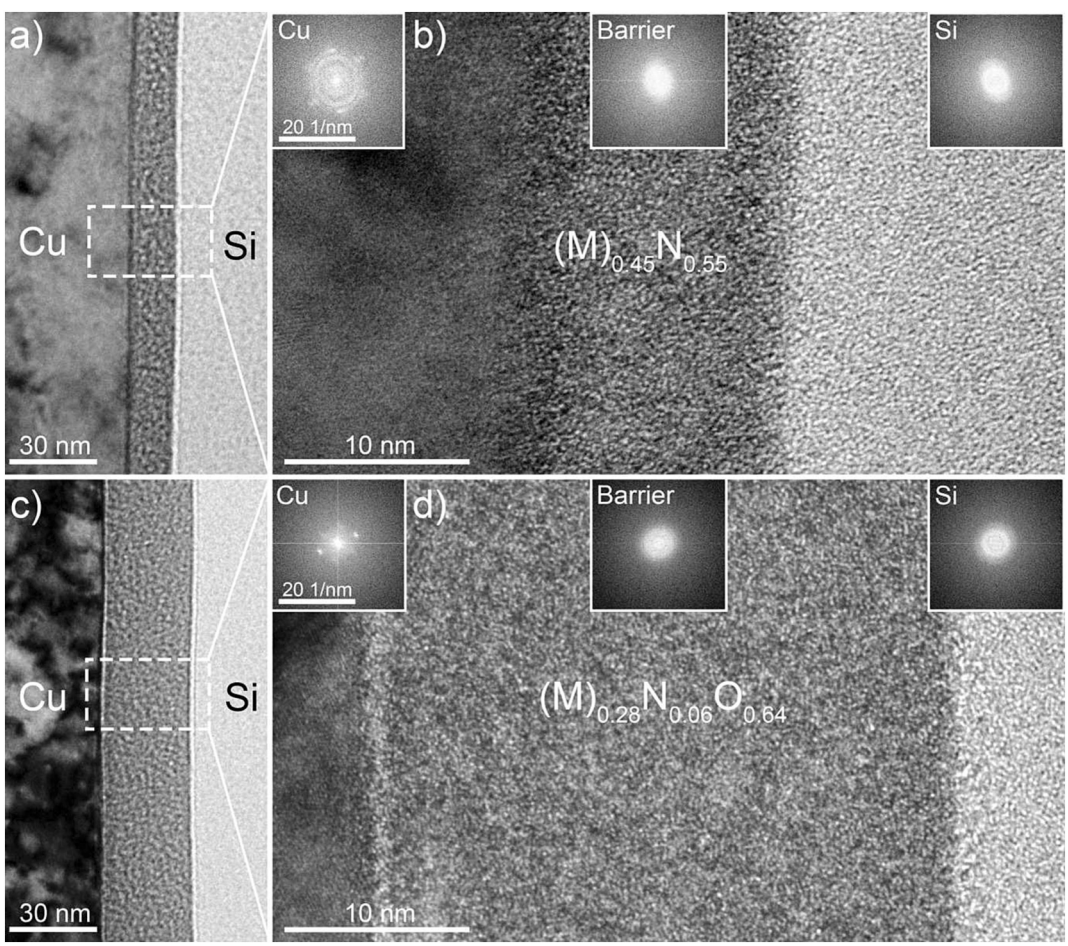

Fig. 2. TEM micrographs with high-resolution inset of the as deposited diffusion stacks with $(Al,Cr,Nb,Ta,Ti)_{0.45}N_{0.55}$ a)-b) and $(Al,Cr,Nb,Ta,Ti)_{0.28}N_{0.06}O_{0.64}$ c)-d) as diffusion barrier (the metals abbreviated as $(M)_x$). The fast Fourier transformations in the insets in b) and d) of regions in the Cu, the diffusion barrier, and the Si from left to right show that the Cu substrate is crystalline, while the other layers are amorphous.

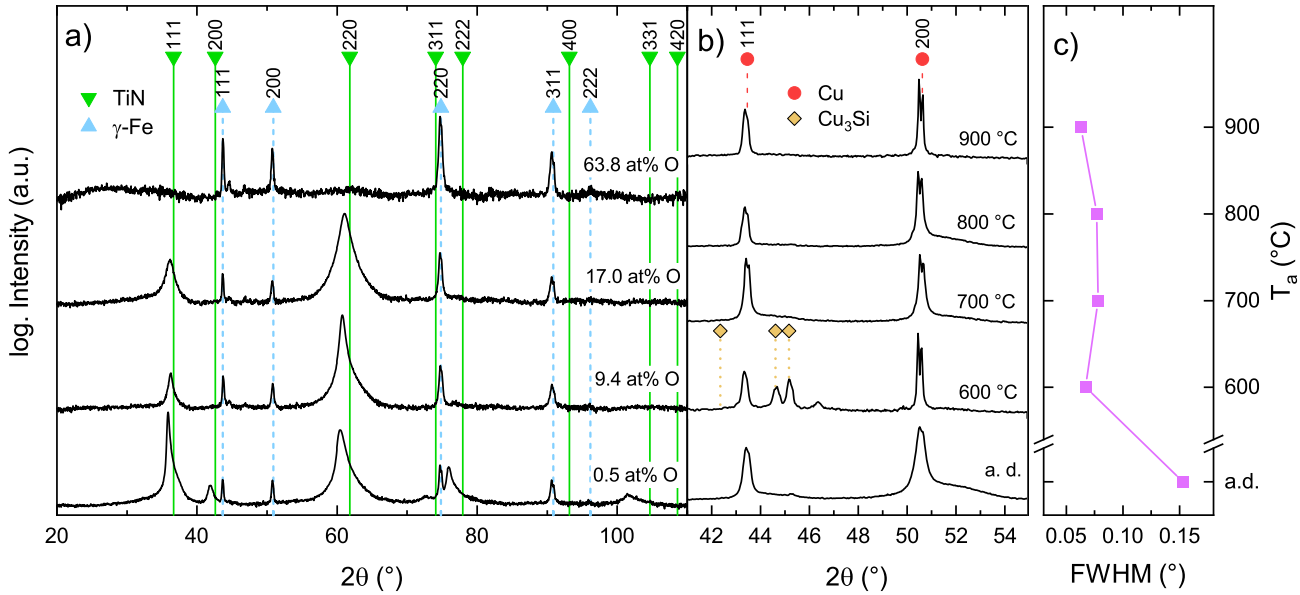

Fig. 3. a) XRD scans of the four barrier materials as ≈1 μm thick coatings on austenite substrates, identified by their oxygen concentrations. b) XRD scans of coated Cu substrates with $(Al,Cr,Nb,Ta,Ti)_{0.45}N_{0.55}$ barriers before and after annealing show the narrowing of peak widths associated with grain growth. c) Full width half maxima of the (200) Cu reflexes in b) after each annealing step. PDF numbers of the references: TiN 00–038-1420, γ-Fe 00–047-1405, Cu 04–009-2090, and Cu_3Si 00–059-0262.

XRD scans of the diffusion stacks before and after annealing show significant grain growth in the Cu substrate during heat treatment, see Fig. 3 b). The Si and diffusion barriers (here $(Al,Cr,Nb,Ta,Ti)_{0.45}N_{0.55}$), initially amorphous as shown by TEM in Fig. 2, remain invisible after annealing. This could be either due to a still amorphous structure, or due to a too small domain size, but the Cu signal is insightful. In as deposited state, both the (111) and (200) reflex appear as single relatively broad peaks. Only the (200) reflex shows a hint of $K\alpha_1$-$K\alpha_2$ separation. After the annealing treatments, the Cu reflexes are distinctly sharper, leading to clearly separated $K\alpha_1$ and $K\alpha_2$ diffraction signals. The full width half maxima (FWHM) of the Cu (200) reflexes, shown in Fig. 3 c), signify the grain growth in the substrate (the annealing temperatures are all $> T_{m,Cu}/2$). In addition, the formation of silicides such as Cu_3Si is visible after annealing to 600 °C, but not after the higher temperatures. This can be explained with the limited Si reservoir and the faster diffusion of Si in Cu at higher temperatures. At higher temperatures the Si is therefore more finely dispersed in the substrate, as will be shown by the SIMS analysis, leading to the formation of smaller domain sizes of eventually crystallizing silicides, which thus become invisible to X-rays.

3.2. Diffusion experiments

Recorded SIMS depth-profiles in HCBU mode of the diffusion stack with the nitride barrier in as deposited state and after annealing to 600 °C for 30 min are shown in Fig. 4 a) and b), respectively. Depth profiles of all other samples and temperatures are redundant for the discussion and are therefore shown in the Supplementary material. The total crater depth for 1800 s of sputtering was determined as roughly 2000 nm in all samples. Since the sputter rate differs strongly between matrices and the thickness of the Si layer is clearly influenced by annealing, the thickness of each individual layer can only be estimated by this method. Measurements of the initial Si layer thickness agree with

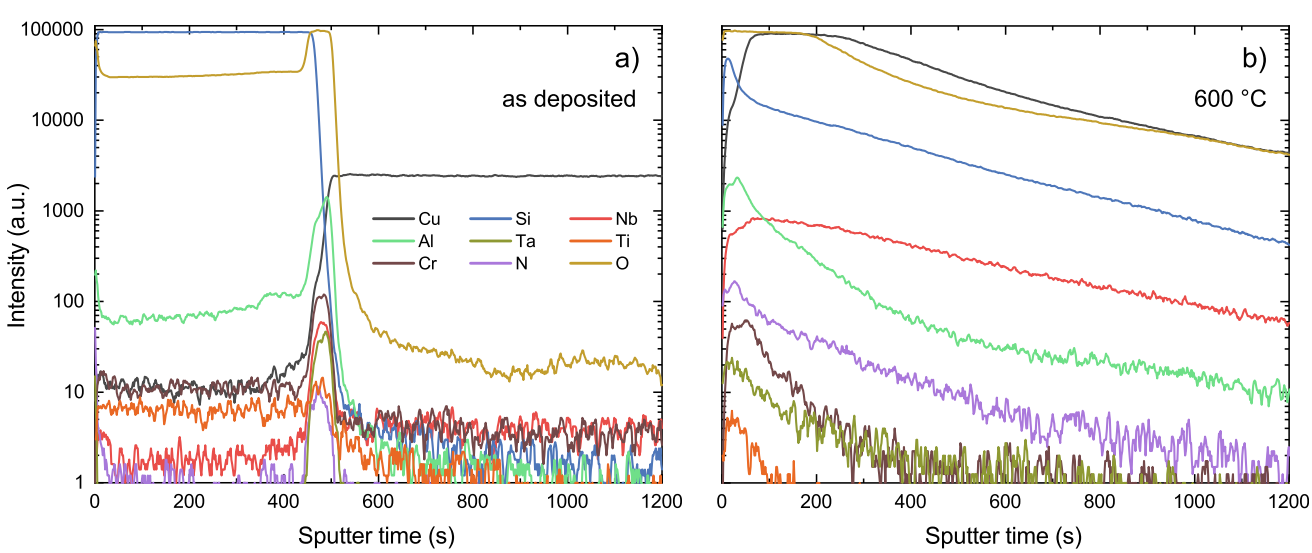

Fig. 4. Depth profiles of the Cu/barrier/Si-stack of the sample with 0.5 at.% O in a) as deposited state and b) after annealing to 600 °C for 30 min, measured by SIMS in high-current-bunched mode.

the TEM investigation. Since a qualitative treatment is sufficient for our discussion, we therefore only show the sputter time. In as deposited state, the sequence of the ≈200 nm thick Si layer (blue line), the diffusion barrier (signified by the peaking metal signals), and the Cu substrate (black line) is clearly visible. This changes drastically even after annealing to the lowest chosen temperature of 600 °C. The outwards Si layer is missing except for a small peak right at the diffusion barrier, while the Si profile in the Cu increases markedly, showing inward diffusion despite the diffusion barrier. This finding correlates to the formation of Cu-silicides, as shown in Fig. 3 b). There, inward diffusion can be seen in all tested samples at all annealing temperatures, without measurable intermetallic phases. At the same time the peaks of the diffusion barrier broaden slightly. Due to the non-quantitative nature of SIMS signals and the matrix effects of a changing chemical environment this broadening is not significant.

The seeming failure of the coating can be explained with the massive grain coarsening of the substrate, shown in Fig. 3 b), which causes localized ruptures of the thin diffusion barrier, leading to rapid inward diffusion of Si. This is demonstrated in Bright-field TEM recordings of the $(Al,Cr,Nb,Ta,Ti)_{0.45}N_{0.55}$ barrier after annealing at 600 Fig. 5 and 900 °C Fig. 5b). The surface of the Cu substrate is visibly warped, and shows voids, which are a sign of Cu out-diffusion (confirmed by Scanning TEM-EDS), but may also have formed during TEM sample preparation. Outside the barrier, the continuous Si layer has vanished into scattered deposits, caused by local disruption of the barrier function. STEM-EDS linescans show that the barrier is still in place, exemplified by the Ti signal (other signals are omitted for better visibility). The Si signal seems to peak within the barrier, but this is a measurement artifact, stemming from the presence of Ta within the barrier, which has a significant overlap with Si in the energy dispersive X-ray spectrum. Due to the much higher fluorescence yield of Ta, and the inability to separate the two elements properly, the Si concentration therefore spikes in the barrier region. Within the Cu matrix, the Si content is too small to be evaluated, STEM-EDS is therefore not a suitable tool to track the movement of Si here. After annealing at 900 °C Fig. 5b), no Si can be found outside the Cu substrate, but the barrier elements are still in place. The seeming increase of Cu in the outer W layer – used as protection for TEM sample preparation by Focused Ion Beam (FIB) – is another measurement artifact, caused by the strong electron scattering within the heavy W (visible as the dark contrast in the bright-field image). This

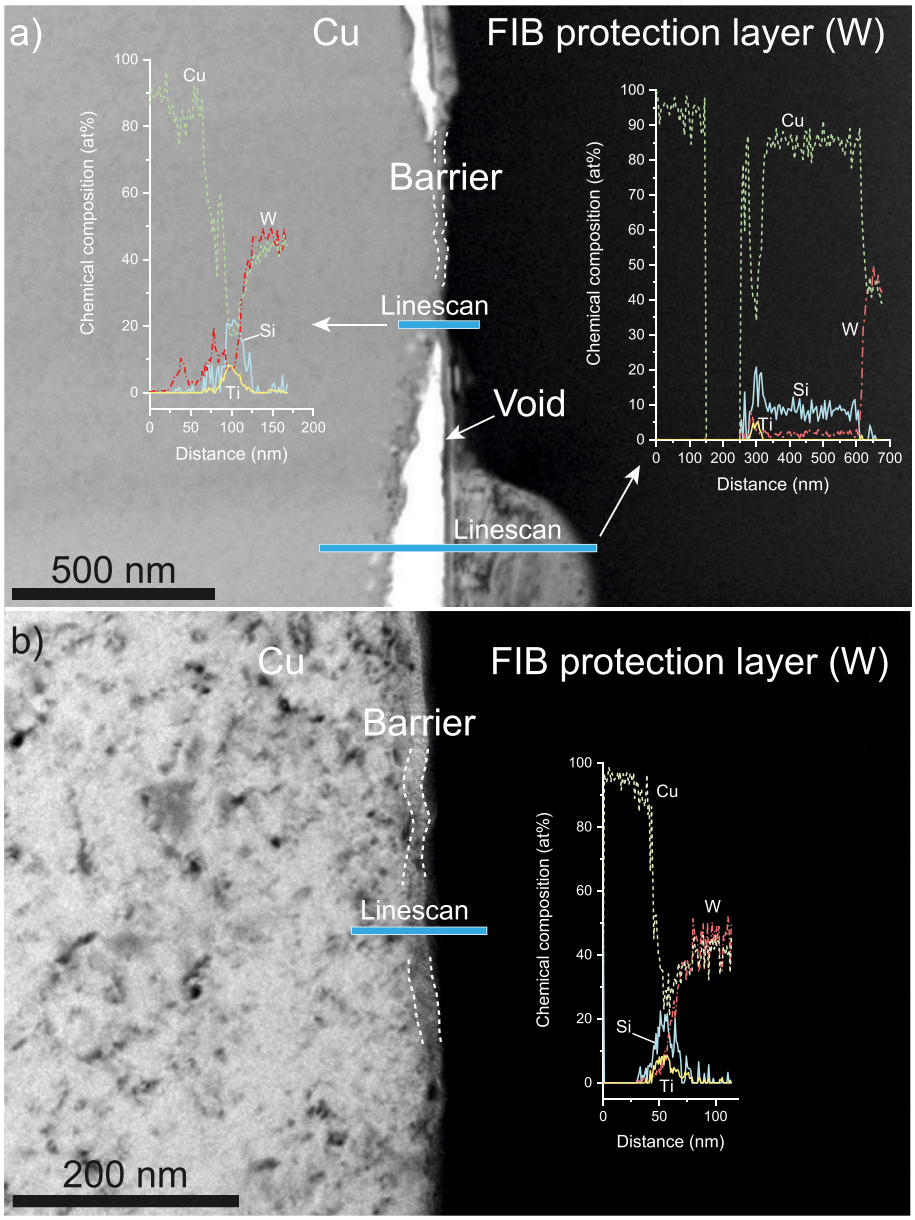

Fig. 5. Bright-field TEM recordings of diffusion stacks with $(Al,Cr,Nb,Ta,Ti)_{0.45}N_{0.55}$ after annealing at 600 a) and 900 °C. a) EDS linescans across the interface show that the barrier is still in place (shown by the Ti signal), but Si deposits are only found in scattered places, mingled by Cu. Since the EDS signals of Si and Ta overlap significantly, with Ta possessing a much higher fluorescence yield, the peaking Si content within the barrier is a measurement artifact and not a sign of actual Si in the barrier. The other EDS signals are not displayed for better visibility. A W layer was added on top of the samples as protection layer during the sample preparation with FIB. b) After annealing at 900 °C, no sign of Si is found outside the Cu substrate. The rising Cu content in the outer W layer is a measurement artifact stemming from radiation scattering in the heavy W, causing fluorescence of the Cu ring that was used to mount the TEM sample.

causes scattered electrons to excite Cu from the ring used to mount the TEM sample.

To separate the performance of the diffusion barrier from this grain growth effect, we recorded the Si positions with lateral resolution, leading to a three-dimensional distribution analysis of the Si. These distributions are shown for all four diffusion barriers and all annealing treatments in Fig. 6. Each light green dot represents one Si count, locations with more than one Si counts are colored in dark green instead. The first five layers are not displayed as surface effects interfere – a common SIMS artifact. The bottom x-y plane in every plot shows via colormap and the associated color bar to its right the average depth of all recorded Si counts for every (x,y) position.

In as deposited state, all samples give a similar picture. The Si is well confined in a ≈100 atomic layers thick film. The colormaps show an even depth distribution with the average depth at ≈50 layers everywhere. Two exceptions are visible in the $(Al,Cr,Nb,Ta,Ti)_{0.39}N_{0.42}O_{0.17}$ and $(Al,Cr,Nb,Ta,Ti)_{0.28}N_{0.06}O_{0.64}$, where local breakthroughs can be seen. Those manifest in columns of Si with average depth distributions of up to 72 and 135 layers, respectively. As those samples have not undergone heat treatments, those breakthroughs must stem from the deposition process. It is possible that imperfections on the polished substrate surface have caused the deposited barrier to form clefts through which the subsequent deposited Si could penetrate into the base material. These defects are rare enough not to disturb the analysis.

After annealing, local breakthrough of Si is evident at all temperatures and through all barrier compositions, like in the unresolved depth profiles in Fig. 4 and in the Supplementary material. The samples annealed at 600 °C stand out, since the Si diffusion seems to have

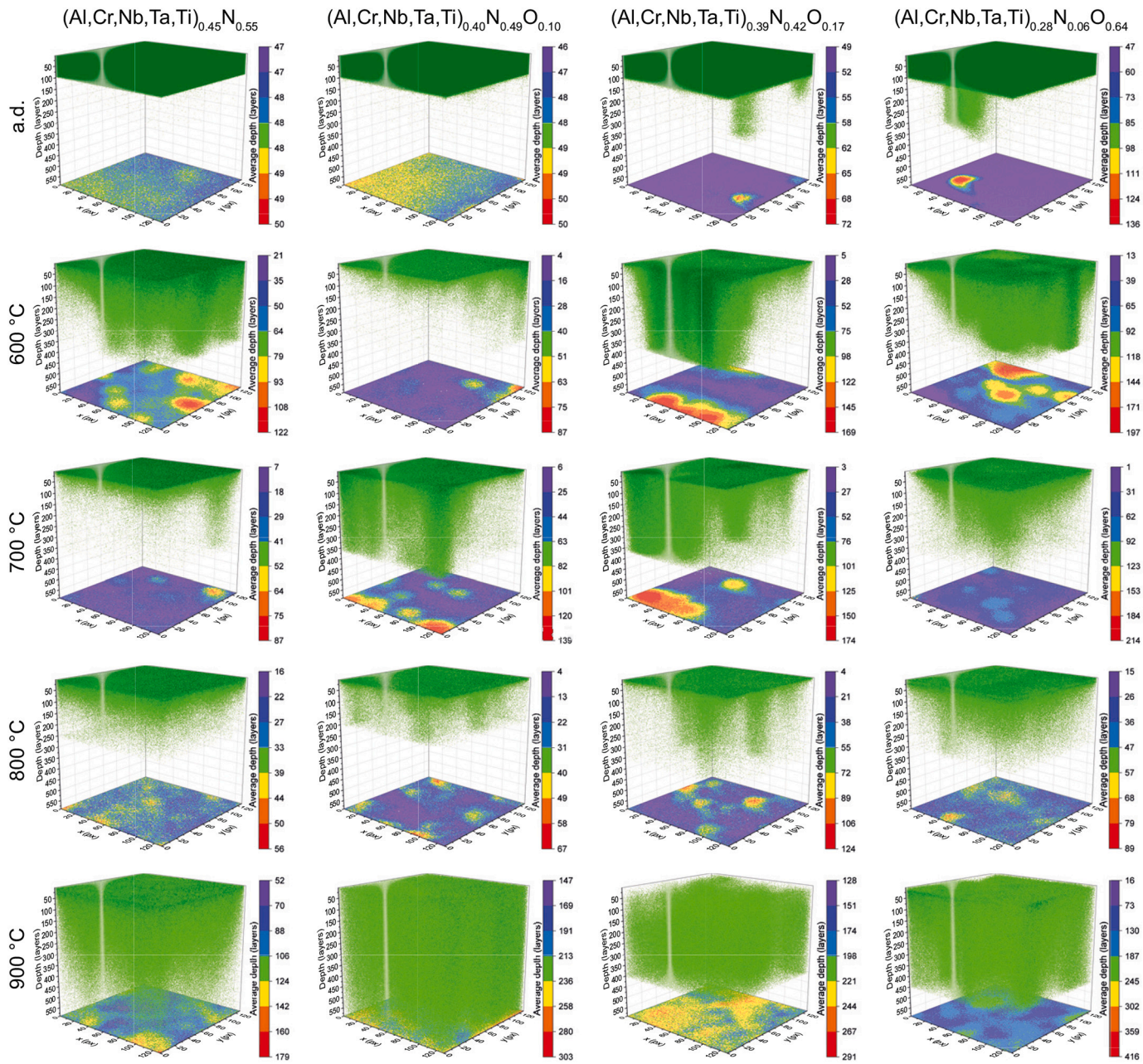

Fig. 6. 3D distribution of Si in the four different Cu/barrier/Si-stack samples in as deposited state (a.d.), and after annealing at 600, 700, 800, and 900 °C for 30 min, measured by SIMS in high-current-bunched (HCBU) mode. The measured area is 100 × 100 μm^2. Higher Si counts are shown in darker color. The first five layers were removed from this display in all samples. The colormap at the bottom of the x-y plane with the respective color scale to its right shows the average depth of recorded Si counts at every x-y-coordinate.

progressed further than in the samples annealed at 700 and 800 °C. The reason for this behavior could be the formation of Cu-silicides (see Fig. 3). Those are not present after annealing at higher temperatures. These silicides could aide rupturing the diffusion barrier, giving the impression of a faster diffusion process. Despite these local penetrations of the diffusion barrier, large regions of the investigated areas still hold the Si back. This is unmistakably shown by the depth distribution colormaps, as well as the fact that a Si reservoir remains at the top of the sample, substantiated by the higher Si counts in dark green (note again that the first five layers are omitted from display). This changes after annealing at 900 °C, where it becomes clear that the barrier function is lost. This becomes apparent by comparison of the depth distribution scale bars at lower annealing temperatures. Both, the lower and upper limit of the average depth of Si counts, increase massively from 800 to 900 °C annealing temperature.

The columnar shape of inwards diffusing Si pockets show that diffusion happens mostly perpendicular to the surface, and relatively little parallel to it, leading to the presumption of grain boundary diffusion. To capture this phenomenon in depth, we recorded the three-dimensional Si distributions of annealed samples with (Al,Cr,Nb,Ta,Ti)$_{0.45}$N$_{0.55}$ and (Al,Cr,Nb,Ta,Ti)$_{0.28}$N$_{0.06}$O$_{0.64}$ diffusion barriers in BA mode at a higher spatial resolution. The distributions can be seen in Fig. 7 with the same colormap in the bottom x-y-plane as in Fig. 6. Due to the superior lateral resolution in BA mode, not every set of (x,y)

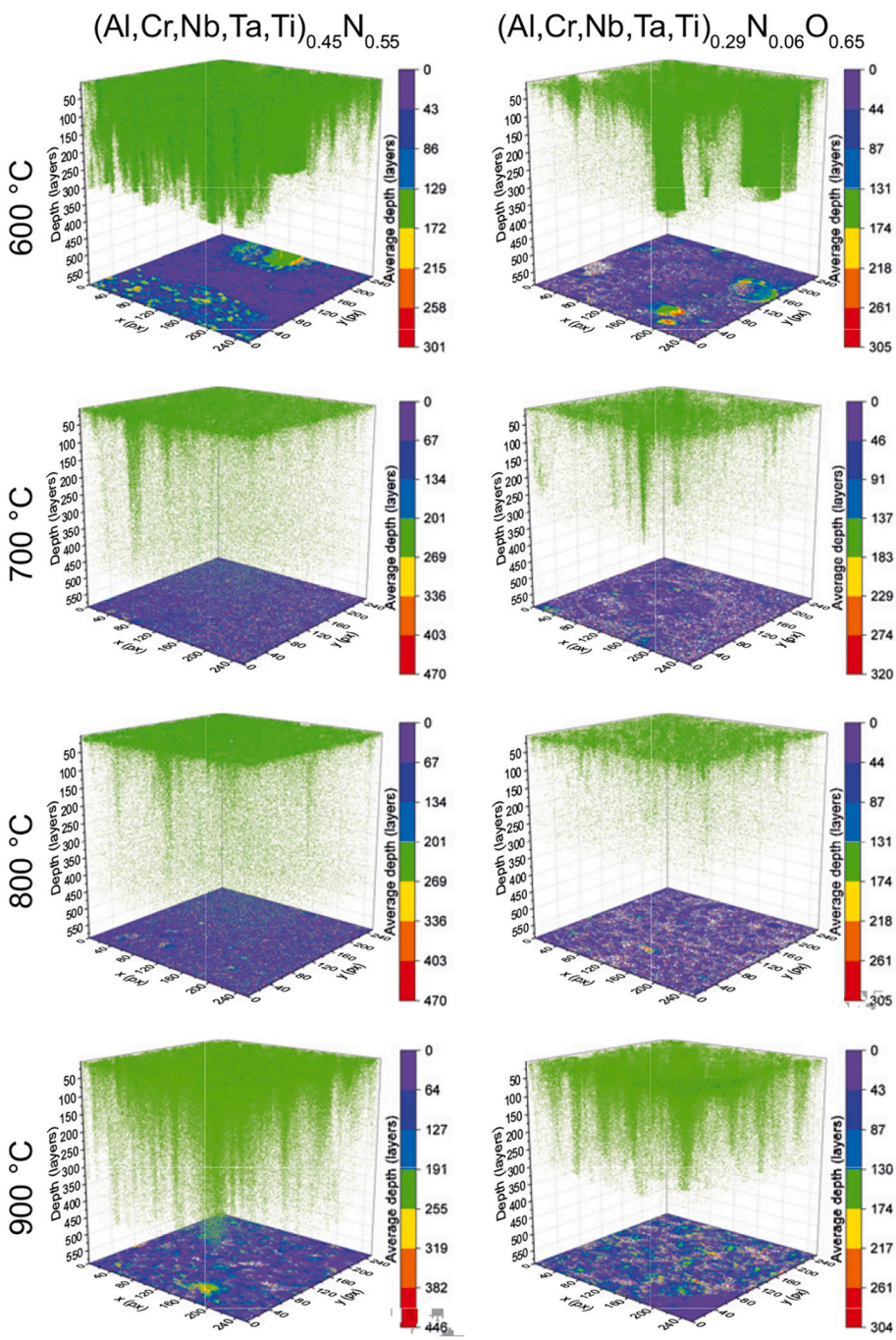

Fig. 7. 3D distribution of Si in the two Cu/barrier/Si-stack samples with the lowest and highest oxygen concentration after annealing at 600, 700, 800, and 900 °C for 30 min, measured by SIMS in burst alignment (BA) mode. The measured area is 100 × 100 μm^2. The first five layers were removed from this display in all samples. The colormap at the bottom of the x-y plane with the respective color scale to its right shows the average depth of recorded Si counts at every x-y-coordinate.

coordinates has an associated Si signal, leading to white regions in the colormap. In comparison to the HCBU mode measurements, the columnar structure of diffusing Si channels is obvious. After the 600 °C annealing treatment, some very broad Si distributions can be seen, several dozen μm in diameter. They are not visible after the other annealing treatments. Endorsed by XRD analysis, we determined that this phenomenon is due to the formation of Cu-silicides, which are not present at the higher temperatures. The formation of these intermetallic phases damages the barrier further, leading to more Si in-diffusion. At 700 and 800 °C, diffusion is essentially only present in localized channels. Due to the very high sensitivity of SIMS, a very dispersed cloud of Si is apparent throughout the substrate. This Si is most likely distributed laterally from the channels and therefore not a sign for barrier failure in general. After annealing to 900 °C, breakthrough in many locations is evident, signifying the loss of the barrier function. In all samples, the $(Al,Cr,Nb,Ta,Ti)_{0.28}N_{0.06}O_{0.64}$ seems to hold the Si back better than the $(Al,Cr,Nb,Ta,Ti)_{0.45}N_{0.55}$, but this can be rationalized from the doubled thickness of the first barrier compared to the latter. Qualitatively, all four tested barriers show a comparable performance.

As the average measurement depth is around 2 μm, the diffusion channels can also be visualized more clearly via cross-sections. Fig. 8 shows these cross-sections from the BA mode measurements from Fig. 7 at four different layers: 5, 50, 100, and 150. Measurements with the $(Al,Cr,Nb,Ta,Ti)_{0.45}N_{0.55}$ barrier are shown in Fig. 8 a), while measurements with the $(Al,Cr,Nb,Ta,Ti)_{0.28}N_{0.06}O_{0.64}$ barrier are shown in Fig. 8 b). To increase the number of visible counts and for a clearer picture, every shown layer was aggregated with the two adjacent layers above and beneath, e.g. "layer 5" contains all Si signals from layers 4–6. Local Si counts > 1 are displayed in darker color. After annealing at 600 °C, large clusters of Si penetrated down to layer 150 and beyond. The coincidence of Si signals is especially apparent in these clusters as seen from the darker color. These Cu-silicide grains are therefore large enough to warrant XRD signals. After annealing to 700 and 800 °C, large Si concentrations are only apparent in the surface-near layer number 5, representing the Si reservoir. Beneath, only very small clusters run through the substrate. Especially after annealing at 900 °C, a broad movement of Si into the Cu is apparent.

The unevenness of the surface, as well as the formation of the Cu-Si grains at the surface, as shown in Fig. 5a), can distort the depth information in our 3D reconstructions. To account for possible distortions in our reconstructions, we display the depth in layers and not in size like the x and y directions. While reducing the fidelity of the reconstruction, these distortions do not change the conclusions of our analysis. Our measurement depth well exceeds the size of the largest of these Cu-Si grains. Therefore, we always measure a significant depth into the Cu substrate. At the temperatures below 900 °C, we can see that the Si intrusion is only local, and stops before the maximum measurement depth. Only at 900 °C a complete barrier failure can be observed.

4. Conclusion

Several other HESN barriers have been reported so far that maintain their barrier function at temperatures up to 800 °C, and fail at 900 °C. The here investigated Al-Cr-Nb-Ta-Ti system enqueues itself in this list.

For the first time in such diffusion studies, we introduced chemical disorder not only on the metal-, but also on the non-metal-sublattice, resulting in 15–30 nm thin barriers with compositions between $(Al,Cr,Nb,Ta,Ti)_{0.45}N_{0.55}$ and $(Al,Cr,Nb,Ta,Ti)_{0.28}N_{0.06}O_{0.64}$. The respective oxynitride and oxide phases demonstrate comparable diffusion retardation to the nitride, but cause a steep increase in resistivity. Structurally, all the films are amorphous as thin films (15–30 nm). Diffractograms of 1 μm thick coatings show that up to 17.0 at.% O can be incorporated in the fcc lattice. Increasing peak widths in as deposited form hint at rising micro-stresses with increasing oxygen content, culminating in a fully amorphous coating with 63.8 at.% O. The application of other non-metals, like B or C, could offer additional design possibilities for future diffusion barrier materials, without the detriment to conductivity.

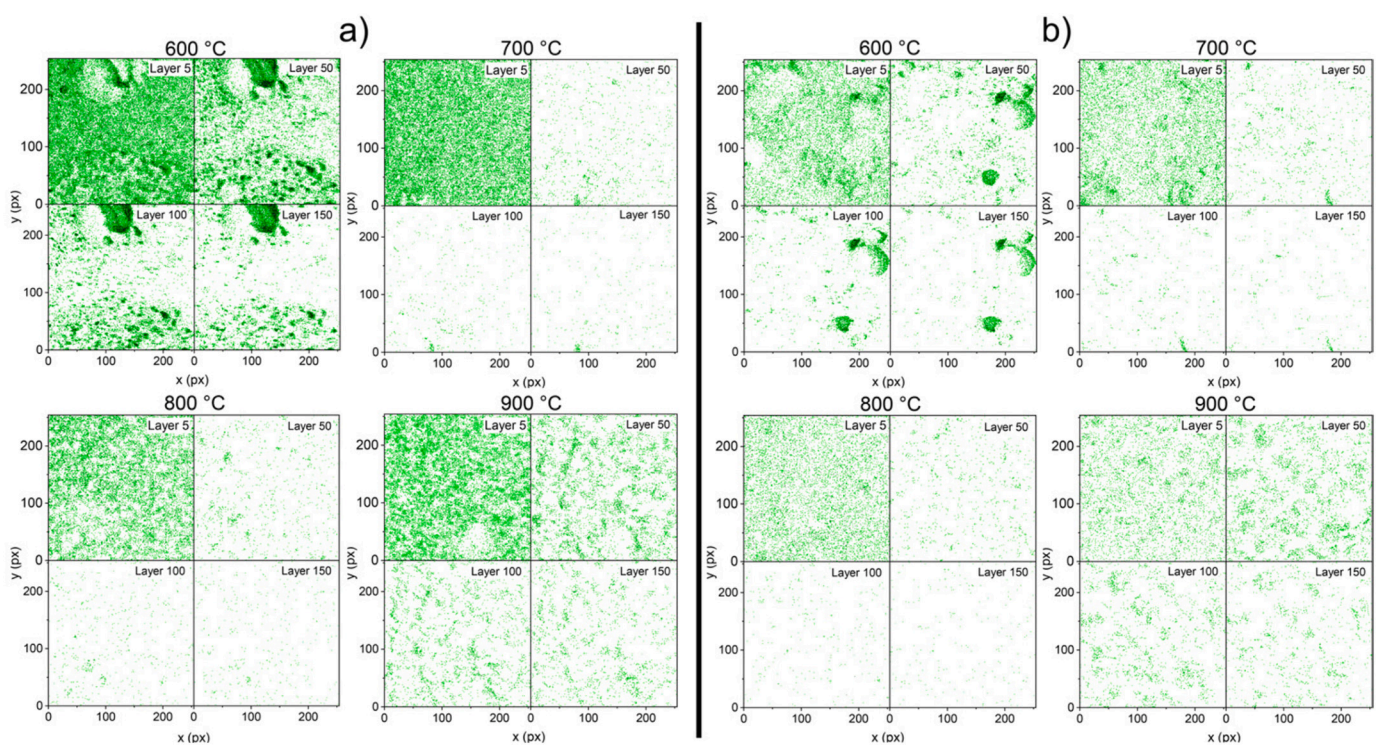

Fig. 8. Cross-sectional view of the the layers 5, 50, 100, and 150, each aggregated with the adjacent layers above and below, of the Si distributions of the samples with $(Al,Cr,Nb,Ta,Ti)_{0.45}N_{0.55}$ a) and $(Al,Cr,Nb,Ta,Ti)_{0.28}N_{0.06}O_{0.64}$ b) as diffusion barriers (shown in Fig. 7 for the whole volume) after annealing at 600, 700, 800, and 900 °C for 30 min. Higher Si counts are shown in darker color.

CRediT authorship contribution statement

Andreas Kretschmer: Conceptualization, Investigation, Methodology, Formal-analysis, Writing-original-draft, Visualization. **Fabian Bohrn:** Investigation, Methodology, Formal-analysis, Writing-original-draft. **Herbert Hutter:** Resources, Supervision, Writing-review-editing. **Eduardo Pitthan:** Investigation, Formal-analysis, Writing-review-editing. **Tuan Thien Tran:** Investigation, Formal-analysis. **Daniel Primetzhofer:** Resources, Formal-analysis, Funding-acquisition, Supervision, Writing-review-editing. **Paul Heinz Mayrhofer:** Resources, Supervision, Project-administration, Funding-acquisition, Writing-original-draft.

Declaration of Competing Interest

The authors declare that they have no known competing financial interests or personal relationships that could have appeared to influence the work reported in this paper.

Data availability

The raw/processed data required to reproduce these findings cannot be shared at this time due to technical or time limitations.

Acknowledgements

This work was funded by the Austrian COMET Program (project K2 InTribology, No. 872176). Support by VR-RFI (#2017–00646_9 and #2019–00191) and the Swedish Foundation for Strategic Research (SSF, contract RIF14-0053) for accelerator operation at Uppsala University is gratefully acknowledged. The authors acknowledge the use of the X-ray center and USTEM at TU Wien. Plansee Composite Materials GmbH is acknowledged for supplying target materials. The authors acknowledge TU Wien Bibliothek for financial support through its Open Access Funding Programme.

Appendix A. Supplementary data

Supplementary data associated with this article can be found, in the online version, athttps://doi.org/10.1016/j.matchar.2023.112676.

References

[1] S.P. Murarka, Multilevel interconnections for ULSI and GSI era, Mater. Sci. Eng. R: Reports 19 (3–4) (1997) 87–151, https://doi.org/10.1016/S0927-796X(97)00002-8.
[2] L. Wang, Z.H. Cao, K. Hu, Q.W. She, X.K. Meng, Effects of electric field annealing on the interface diffusion of Cu/Ta/Si stacks, Appl. Surf. Sci. 257 (24) (2011) 10845–10849, https://doi.org/10.1016/j.apsusc.2011.07.119.
[3] Z.H. Cao, K. Hu, X.K. Meng, Diffusion barrier properties of amorphous and nanocrystalline Ta films for Cu interconnects, J. Appl. Phys. 106 (11) (2009), https://doi.org/10.1063/1.3266164.
[4] S. Rawal, D.P. Norton, T.J. Anderson, L. McElwee-White, Properties of W-Ge-N as a diffusion barrier material for Cu, Appl. Phys. Lett. 87 (11) (2005), https://doi.org/10.1063/1.2042534.
[5] T. Kouno, H. Niwa, M. Yamada, Effect of TiN Microstructure on Diffusion Barrier Properties in Cu Metallization, J. Electrochem. Soc. 145 (6) (1998) 2164–2167, https://doi.org/10.1149/1.1838612.
[6] M.H. Tsai, S.C. Sun, C.E. Tsai, S.H. Chuang, H.T. Chiu, Comparison of the diffusion barrier properties of chemical-vapor-deposited TaN and sputtered TaN between Cu and Si, J. Appl. Phys. 79 (9) (1996) 6932–6938, https://doi.org/10.1063/1.361518.
[7] Y. Meng, Z.X. Song, J.H. Chen, F. Ma, Y.H. Li, J.F. Wang, C.C. Wang, K.W. Xu, Ultrathin ZrBxOy films as diffusion barriers in Cu interconnects, Vacuum 119 (2015) 1–6, https://doi.org/10.1016/j.vacuum.2015.04.026.
[8] L. Wang, Z.H. Cao, K. Hu, Q.W. She, X.K. Meng, Improved diffusion barrier performance of Ru/TaN bilayer by N effusion in TaN underlayer, Mater. Chem. Phys. 135 (2–3) (2012) 806–809, https://doi.org/10.1016/j.matchemphys.2012.05.061.
[9] S.Y. Chang, C.Y. Wang, M.K. Chen, C.E. Li, Ru incorporation on marked enhancement of diffusion resistance of multi-component alloy barrier layers, J. Alloy. Compd. 509 (5) (2011) L85–L89, https://doi.org/10.1016/j.jallcom.2010.11.124.
[10] J.-W. Yeh, S.-K. Chen, S.-J. Lin, J.-Y. Gan, T.-S. Chin, T.-T. Shun, C.-H. Tsau, S.-Y. Chang, Nanostructured High-Entropy Alloys with Multiple Principal Elements: Novel Alloy Design Concepts and Outcomes, Adv. Eng. Mater. 6 (5) (2004) 299–303, https://doi.org/10.1002/adem.200300567.
[11] B. Cantor, I.T. Chang, P. Knight, A.J. Vincent, Microstructural development in equiatomic multicomponent alloys, Mater. Sci. Eng., A 375–377 (1-2 SPEC. ISS.) (2004) 213–218, https://doi.org/10.1016/j.msea.2003.10.257.
[12] J.-W. Yeh, Recent Progress in High-entropy Alloys, Ann. Chim. – Sci. Mater. 31 (2006) 633–648.
[13] D.B. Miracle, O.N. Senkov, A critical review of high entropy alloys and related concepts, Acta Mater. 122 (2017) 448–511, https://doi.org/10.1016/j.actamat.2016.08.081.
[14] J. Dbrowa, M. Zajusz, W. Kucza, G. Cieślak, K. Berent, T. Czeppe, T. Kulik, M. Danielewski, Demystifying the sluggish diffusion effect in high entropy alloys, J. Alloy. Compd. 783 (2019) 193–207, https://doi.org/10.1016/j.jallcom.2018.12.300.
[15] X. Li, J. Zhang, D. Cui, X. Luo, H. Wang, Effects of Fe, Cr and Mn on inter-diffusion in CoNi-containing multiple principal alloys, Intermetallics 140 (October 2021) (2022), 107400, https://doi.org/10.1016/j.intermet.2021.107400.
[16] Y.-Z. Wang, Y.-J. Wang, Disentangling diffusion heterogeneity in high-entropy alloys, Acta Mater. 224 (2022), 117527, https://doi.org/10.1016/j.actamat.2021.117527.
[17] A. Kretschmer, D. Holec, K. Yalamanchili, H. Rudigier, M. Hans, J.M. Schneider, P. H. Mayrhofer, Strain-stabilized Al-containing high-entropy sublattice nitrides, Acta Mater. 224 (2022), 117483, https://doi.org/10.1016/j.actamat.2021.117483.
[18] G. Gottstein, Materialwissenschaft und Werkstofftechnik, Springer-Lehrbuch, Springer Berlin Heidelberg, Berlin, Heidelberg, 2014.
[19] D.C. Tsai, Y.L. Huang, S.R. Lin, D.R. Jung, S.Y. Chang, F.S. Shieu, Diffusion barrier performance of TiVCr alloy film in Cu metallization, Appl. Surf. Sci. 257 (11) (2011) 4923–4927, https://doi.org/10.1016/j.apsusc.2010.12.149.
[20] M.-H. Tsai, C.-W. Wang, C.-W. Tsai, W.-J. Shen, J.-W. Yeh, J.-Y. Gan, W.-W. Wu, Thermal Stability and Performance of NbSiTaTiZr High-Entropy Alloy Barrier for Copper Metallization, J. Electrochem. Soc. 158 (11) (2011) H1161, https://doi.org/10.1149/2.056111jes.
[21] M.H. Tsai, J.W. Yeh, J.Y. Gan, Diffusion barrier properties of AlMoNbSiTaTiVZr high-entropy alloy layer between copper and silicon, Thin Solid Films 516 (16) (2008) 5527–5530, https://doi.org/10.1016/j.tsf.2007.07.109.
[22] P. Kumar, S. Avasthi, Diffusion barrier with 30-fold improved performance using AlCrTaTiZrN high-entropy alloy, J. Alloy. Compd. 814 (2020), 151755, https://doi.org/10.1016/j.jallcom.2019.151755.
[23] A. Kirnbauer, A. Kretschmer, C.M. Koller, T. Wojcik, V. Paneta, M. Hans, J. M. Schneider, P. Polcik, P.H. Mayrhofer, Mechanical properties and thermal stability of reactively sputtered multi-principal-metal Hf-Ta-Ti-V-Zr nitrides, Surf. Coat. Technol. 389 (2020), 125674, https://doi.org/10.1016/j.surfcoat.2020.125674.
[24] J.M. Schneider, How high is the entropy in high entropy ceramics? J. Appl. Phys. 130 (15) (2021) https://doi.org/10.1063/5.0062523.
[25] R. Li, B. Qiao, H. Shang, J. Zhang, C. Jiang, W. Zhang, Multi-component AlCrTaTiZrMo-nitride film with high diffusion resistance in copper metallization, J. Alloy. Compd. 748 (2018) 258–264, https://doi.org/10.1016/j.jallcom.2018.03.084.
[26] M.H. Tsai, C.W. Wang, C.H. Lai, J.W. Yeh, J.Y. Gan, Thermally stable amorphous (AlMoNbSiTaTiVZr)50N50 nitride film as diffusion barrier in copper metallization, Appl. Phys. Lett. 92 (5) (2008) 90–93, https://doi.org/10.1063/1.2841810.
[27] S.-Y. Chang, Y.-C. Huang, C.-E. Li, H.-F. Hsu, J.-W. Yeh, S.-J. Lin, Improved Diffusion-Resistant Ability of Multicomponent Nitrides: From Unitary TiN to Senary High-Entropy (TiTaCrZrAlRu)N, JOM 65 (12) (2013) 1790–1796, https://doi.org/10.1007/s11837-013-0676-2.
[28] S.-Y. Chang, M.-K. Chen, D.-S. Chen, Multiprincipal-Element AlCrTaTiZr-Nitride Nanocomposite Film of Extremely High Thermal Stability as Diffusion Barrier for Cu Metallization, J. Electrochem. Soc. 156 (5) (2009) G37, https://doi.org/10.1149/1.3097186.
[29] S.C. Liang, D.C. Tsai, Z.C. Chang, T.N. Lin, M.H. Shiao, F.S. Shieu, Thermally stable TiVCrZrHf nitride films as diffusion barriers in copper metallization, Electrochem. Solid-State Lett. 15 (1) (2021), https://doi.org/10.1149/2.012201esl.
[30] S.Y. Chang, D.S. Chen, 10-nm-thick quinary (AlCrTaTiZr)N film as effective diffusion barrier for Cu interconnects at 900c, Appl. Phys. Lett. 94 (23) (2009) 2007–2010, https://doi.org/10.1063/1.3155196.
[31] R. Li, M. Li, C. Jiang, B. Qiao, W. Zhang, J. Xu, Thermal stability of AlCrTaTiZrMo-nitride high entropy film as a diffusion barrier for Cu metallization, J. Alloy. Compd. 773 (2019) 482–489, https://doi.org/10.1016/j.jallcom.2018.09.283.
[32] S.-Y. Chang, D.-S. Chen, Ultra-Thin (AlCrTaTiZr)N x/AlCrTaTiZr Bilayer Structures of High Diffusion Resistance to Cu Metallization, ECS Trans. 28 (2) (2019) 361–372, https://doi.org/10.1149/1.3372591.
[33] S.Y. Chang, C.E. Li, S.C. Chiang, Y.C. Huang, 4-nm thick multilayer structure of multi-component (AlCrRuTaTiZr)N x as robust diffusion barrier for Cu interconnects, J. Alloy. Compd. 515 (2012) 4–7, https://doi.org/10.1016/j.jallcom.2011.11.082.
[34] R. Li, T. Chen, C. Jiang, J. Zhang, Y. Zhang, P.K. Liaw, Applications of High Diffusion Resistance Multi-component AlCrTaTiZrRu/(AlCrTaTiZrRu)N 0.7 Film in Cu Interconnects, Adv. Eng. Mater. 22 (11) (2020), 2000557, https://doi.org/10.1002/adem.202000557.
[35] P.F. Li, Y.J. Ma, H. Ma, S.W. Ta, Z. Yang, X.T. Han, M.J. Kai, J.H. Chen, Z.H. Cao, Enhanced diffusion barrier property of nanolayered NbMoTaW/TiVCr high entropy alloy for copper metallization, J. Alloy. Compd. 895 (2022), https://doi.org/10.1016/j.jallcom.2021.162574.

[36] D.M. Holzapfel, D. Music, M. Hans, S. Wolff-Goodrich, D. Holec, D. Bogdanovski, M. Arndt, A.O. Eriksson, K. Yalamanchili, D. Primetzhofer, C.H. Liebscher, J. M. Schneider, Enhanced thermal stability of (Ti, Al)N coatings by oxygen incorporation, Acta Mater. 218 (2021), 117204, https://doi.org/10.1016/j.actamat.2021.117204.

[37] A. Kretschmer, A. Kirnbauer, V. Moraes, D. Primetzhofer, K. Yalamanchili, H. Rudigier, P.H. Mayrhofer, Improving phase stability, hardness, and oxidation resistance of reactively magnetron sputtered (Al, Cr, Nb, Ta, Ti)N thin films by Si-alloying, Surf. Coat. Technol. 416 (February) (2021), 127162, https://doi.org/10.1016/j.surfcoat.2021.127162.

[38] A. Kirnbauer, C. Spadt, C.M. Koller, S. Kolozsvári, P.H. Mayrhofer, High-entropy oxide thin films based on Al–Cr–Nb–Ta–Ti, Vacuum 168 (July) (2019), 108850, https://doi.org/10.1016/j.vacuum.2019.108850.

[39] P. Ström, P. Petersson, M. Rubel, G. Possnert, A combined segmented anode gas ionization chamber and time-of-flight detector for heavy ion elastic recoil detection analysis, Rev. Sci. Instrum. 87 (10) (2016), 103303, https://doi.org/10.1063/1.4963709.

[40] H.Y. Qu, D. Primetzhofer, M.A. Arvizu, Z. Qiu, U. Cindemir, C.G. Granqvist, G. A. Niklasson, Electrochemical Rejuvenation of Anodically Coloring Electrochromic Nickel Oxide Thin Films, ACS Appl. Mater. Interfaces 9 (49) (2017) 42420–42424, https://doi.org/10.1021/acsami.7b13815.

[41] M.V. Moro, R. Holeňák, L. Zendejas Medina, U. Jansson, D. Primetzhofer, Accurate high-resolution depth profiling of magnetron sputtered transition metal alloy films containing light species: A multi-method approach, Thin Solid Films 686 (January) (2019), https://doi.org/10.1016/j.tsf.2019.137416.

[42] E. Pitthan, M. Moro, S. Corrêa, D. Primetzhofer, Assessing boron quantification and depth profiling of different boride materials using ion beams, Surf. Coat. Technol. 417 (April) (2021), 127188, https://doi.org/10.1016/j.surfcoat.2021.127188.

[43] A. Benninghoven, Surface analysis by Secondary Ion Mass Spectrometry (SIMS), Surf. Sci. 299–300 (C) (1994) 246–260, https://doi.org/10.1016/0039-6028(94)90658-0.

[44] A. Benninghoven, Chemical Analysis of Inorganic and Organic Surfaces and Thin Films by Static Time-of-Flight Secondary Ion Mass Spectrometry (TOF-SIMS), Angew. Chem. Int. Ed. Engl. 33 (10) (1994) 1023–1043, https://doi.org/10.1002/anie.199410231.

[45] R.N. Sodhi, Time-of-flight secondary ion mass spectrometry (TOF-SIMS): - Versatility in chemical and imaging surface analysis, Analyst 129 (6) (2004) 483–487, https://doi.org/10.1039/b402607c.

[46] M. Kubicek, G. Holzlechner, A.K. Opitz, S. Larisegger, H. Hutter, J. Fleig, A novel ToF-SIMS operation mode for sub 100 nm lateral resolution: Application and performance, Appl. Surf. Sci. 289 (2014) 407–416, https://doi.org/10.1016/j.apsusc.2013.10.177.